Supplemental Material

The 2019 Southern Hemisphere stratospheric polar vortex weakening and its impacts

Eun-Pa Lim[1], Harry H. Hendon[1], Amy H. Butler[2], David W. J. Thompson[3], Zachary Lawrence[4], Adam A. Scaife[5,6], Theodore G. Shepherd[7], Inna Polichtchouk[8], Hisashi Nakamura[9], Chiaki Kobayashi[10], Ruth Comer[5], Lawrence Coy[11,12], Andrew Dowdy[1], Rene D. Garreaud[13], Paul A. Newman[11], and Guomin Wang[1].

[1] Bureau of Meteorology, Melbourne, Australia

[2] NOAA Chemical Sciences Laboratory, Boulder, Colorado, USA

[3] Department of Atmospheric Science, Colorado State University, Fort Collins, Colorado, USA

[4] NOAA Physical Sciences Laboratory, Boulder, Colorado, USA

[5] Met Office Hadley Centre, Exeter, UK

[6] College of Engineering, Mathematics and Physical Sciences, University of Exeter, UK

[7] Department of Meteorology, University of Reading, Reading, UK

[8] European Centre for Medium-Range Weather Forecasts, Reading, UK

[9] Research Center for Advanced Science and Technology, University of Tokyo, Japan

[10] Meteorological Research Institute, Japan Meteorological Agency, Tsukuba, Japan

[11] NASA Goddard Space Flight Center, Greenbelt, Maryland, USA

[12] Science Systems and Applications, Inc., Lanham, Maryland, USA

[13] Department of Geophysics, University of Chile, Chile

Corresponding author: eun-pa.lim@bom.gov.au

Regression analysis

The syntheses (or reconstructions) of the 2019 anomalies, derived from regression analysis, are computed by the following two steps:

Step 1)

The regression is computed for the training period 1979-2018:

$$\hat{y}_t = \sum b_i x_{i,t}$$

where *t* and *i* denote the training period and the number of predictors, respectively; $\hat{y}_t$ is the synthesis of the predictand *y*; b_i is the regression coefficient of the i^{th} predictor, derived from least squares fit regression; and $x_{i,t}$ is the time series of the i^{th} predictor.

Step 2)

The synthesis for 2019 is computed using the b_i derived from the training period and multiplied by the predictor values during 2019:

$$\hat{y}_{2019} = \sum b_i x_{i,2019}$$

Figures 3, 4, and 6 and Supplementary Figures S2, S5-7, and S9 are based on univariate regression while Figures 7 and 8 are based on multiple linear regression.

Figures

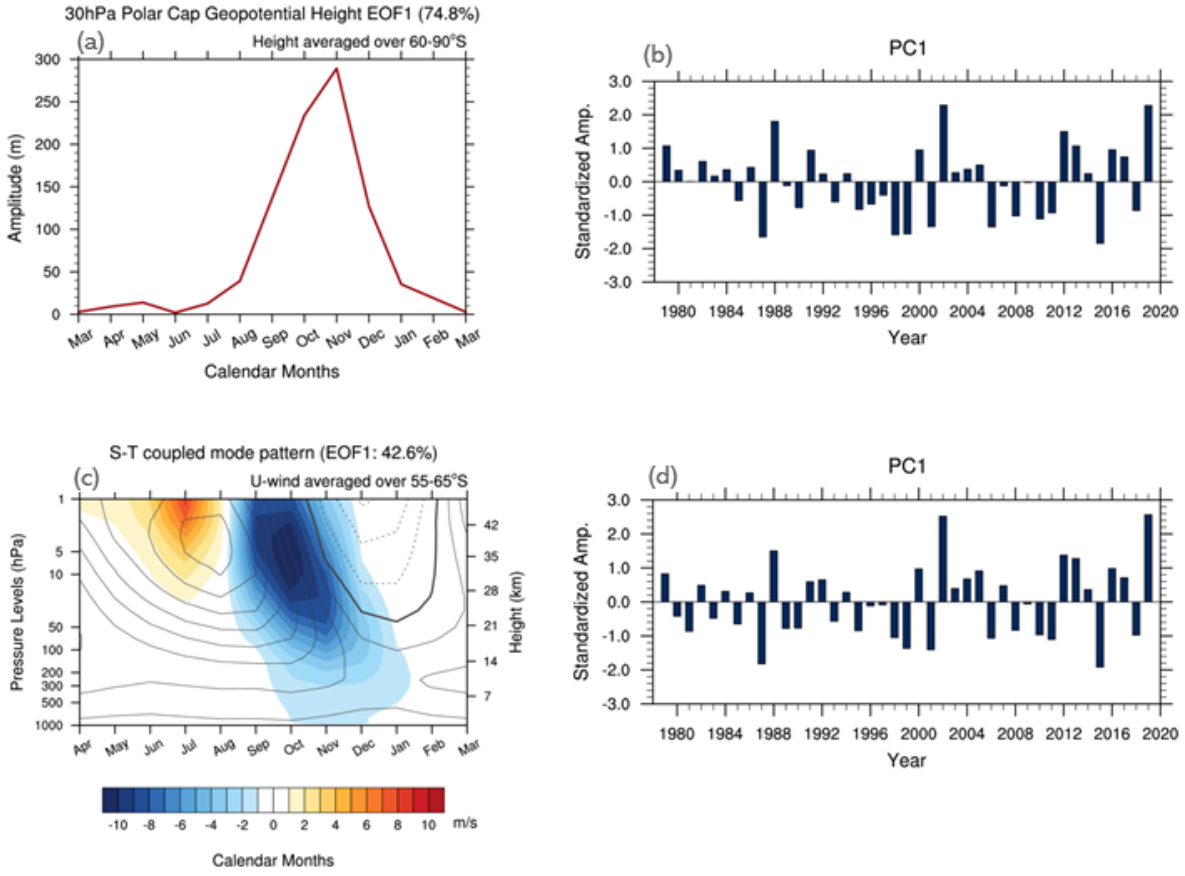

FIG S1. (a) Eigenvector and (b) expansion coefficients of the leading mode of the multiple empirical orthogonal function (EOF) of the Antarctic polar cap (60-90°S) geopotential height variability at the 30 hPa level as described in Byrne and Shepherd (2018) (their Figures 3b and 4). The EOF analysis was applied to the data over 1979-2018, and 2019-2020 data were projected onto the eigenvector to get the 2019 PC1 anomaly. A linear trend was removed from the geopotential height data before the EOF analysis. (c),(d) Same as (a),(b) but the leading mode of the height-time domain EOF of the Antarctic subpolar (55-65°S) zonal-mean zonal wind variability as described in Lim et al. (2018) (their Figures 3a,b). Lim et al. (2018) referred to this mode as the stratosphere-troposphere coupled mode. As there is no significant linear trend in PC1 of the stratosphere-troposphere coupled mode, raw zonal-mean zonal wind data were used for (c) and (d). As described in the main article, the amplitudes of 2019 are on a par with those of 2002 in both PC1 timeseries.

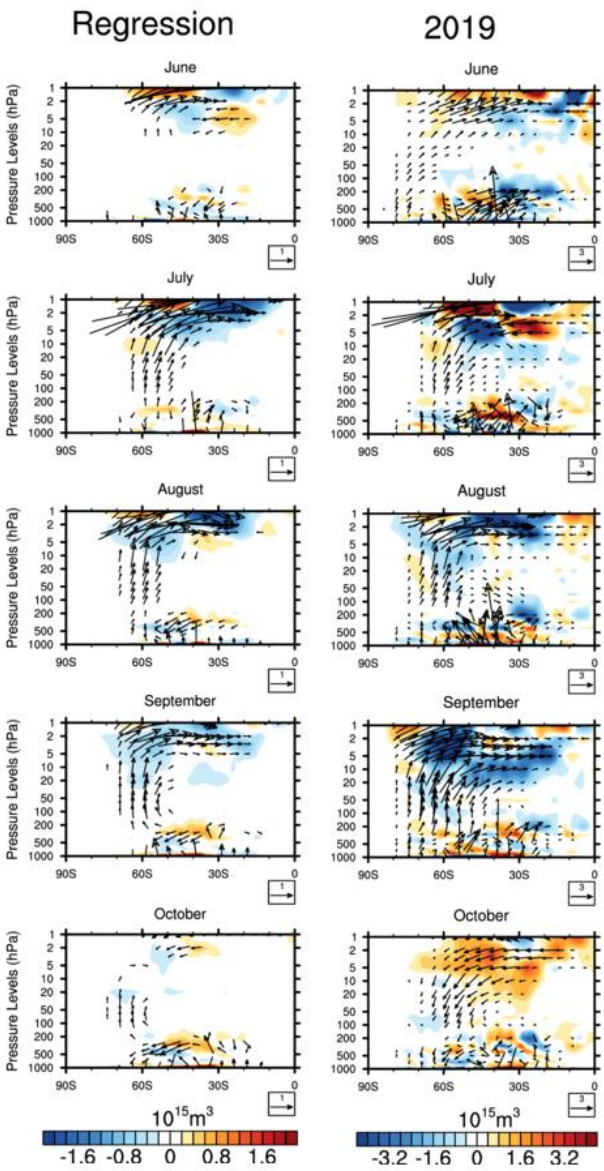

FIG S2. (Left panels) Syntheses of the monthly anomalies of E-P flux (vectors) and E-P flux divergence (shading) for 2019 based on regression onto the September to November mean zonal-mean zonal wind anomalies at 60°S, 10 hPa (i.e., the stratospheric polar vortex index; SPVI; Fig 2b in the main article); and (right panels) the 2019 observed anomalies relative to the respective climatologies of 1979-2018. The E-P flux vector scale unit is 10^{15} m^3 in horizontal direction and 10^{17} $m^3 \cdot kPa$ in vertical direction, and the reference vector scale is 1 in the left panels and 3 in the right panels. The vectors were scaled by the inverse square root of pressure, taking 100 hPa as a reference first and then scaled by 2 below the 10-hPa level for improved visibility of vectors. Vectors with magnitudes less than 0.2 are not displayed. The color shading interval is $0.2 \times 10^{15} m^3$ in the left panels and $0.4 \times 10^{15} m^3$ in the right panels. E-P flux and divergence calculations follow Peixoto and Oort (1992), using the JRA-55 reanalysis set of instantaneous daily (00Z) data of zonal and meridional winds and temperature. Syntheses of the E-P flux and its divergence for 2019 were obtained as described in the first section of this document.

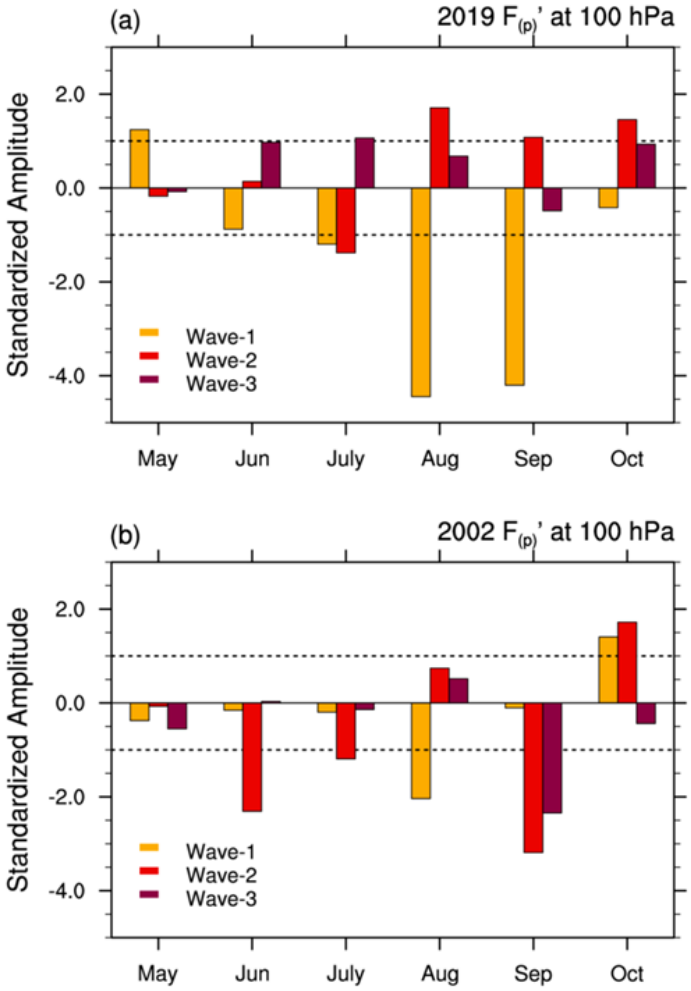

FIG S3. Standardized northward eddy heat flux anomalies of wave-1, wave-2 and wave-3 in (a) 2019 and (b) 2002 at 100 hPa. The negative sign indicates increased poleward heat flux. While wave-1 heat flux anomalies were dominant in August and September 2019, there was greater than |1σ| amplitude of wave-2 northward heat flux in July, which was comparable to that of wave-1 in the same month. In 2002, there were large wave-2 heat flux anomalies observed during June, July, and September, while wave-1 only made a substantial contribution in August (e.g., Harnik et al. 2005; Newman and Nash 2005).

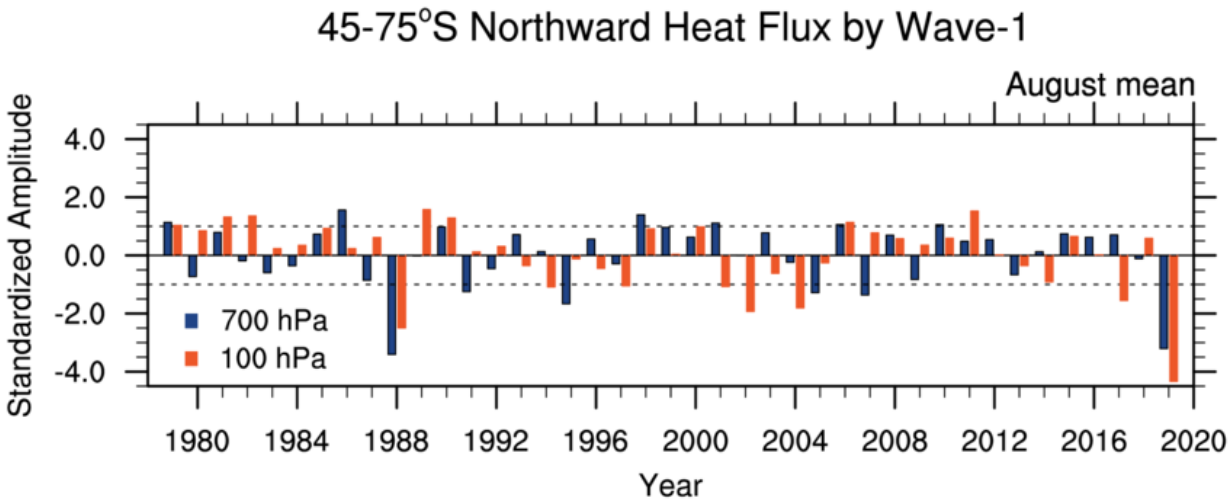

FIG S4. Time series of the August-mean northward wave-1 heat flux anomalies averaged over 45-75°S at 700 hPa (blue colored bars) and 100 hPa (orange colored bars). The negative sign indicates increased poleward heat flux. The northward heat flux anomaly in 2019 was the 2nd most negative at 700 hPa after that of 1988 while it was the most negative at 100 hPa.

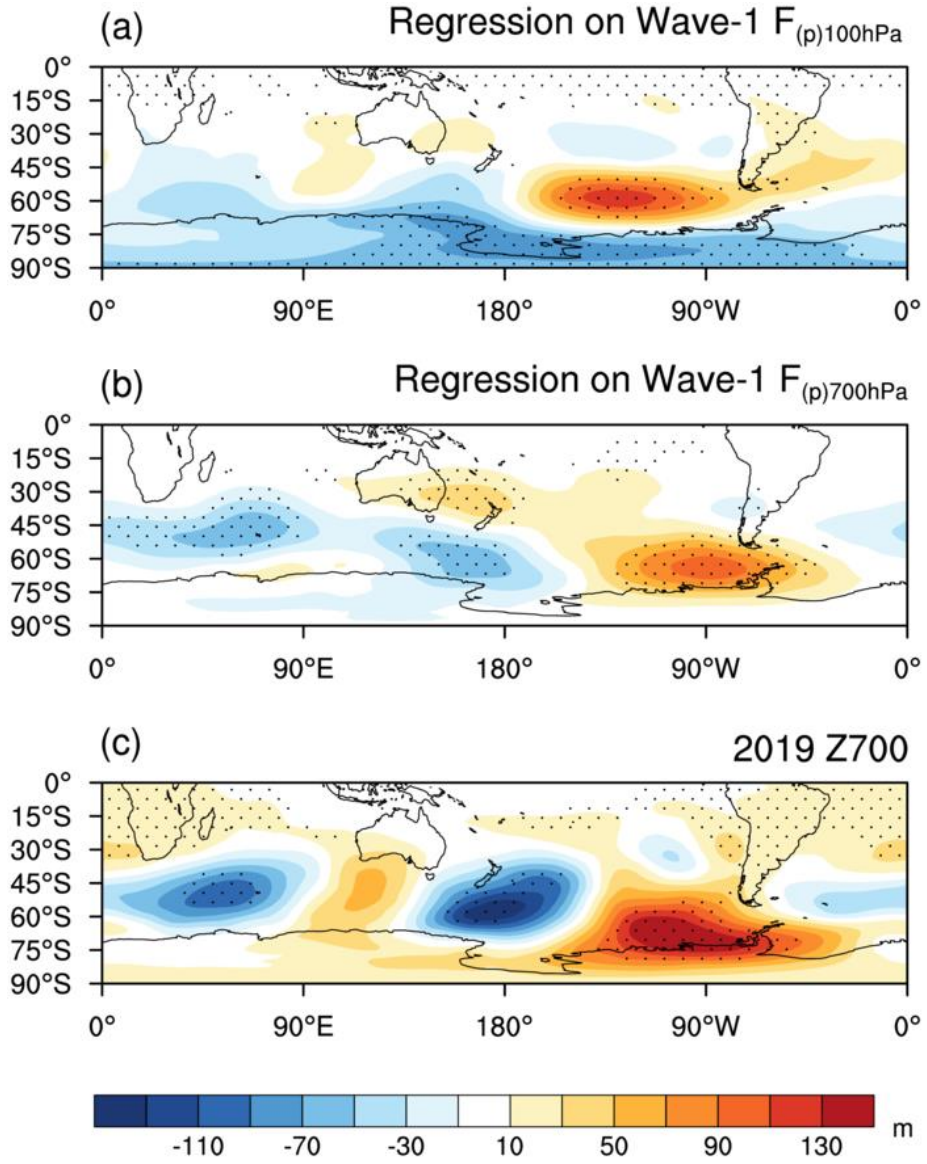

FIG S5. Syntheses of the 2019 August-mean 700 hPa geopotential height (Z700) anomalies derived from the regression onto the August-mean northward wave-1 heat flux at (a) 100 hPa and (b) at 700 hPa. The northward heat fluxes (the predictors) were averaged 45-75°S. Syntheses of the 2019 Z700 anomalies were generated as described in the first section of this document. (c) The observed Z700 anomalies for August 2019. The color shading interval is 20 m. Stippling in (a) and (b) indicates the statistical significance of the regression coefficients at the 10% level, assessed by a two-tailed Student t-test with 40 samples. Stippling in (c) indicates the anomalies at the 5% tails of the climatological distribution of 1979-2018.

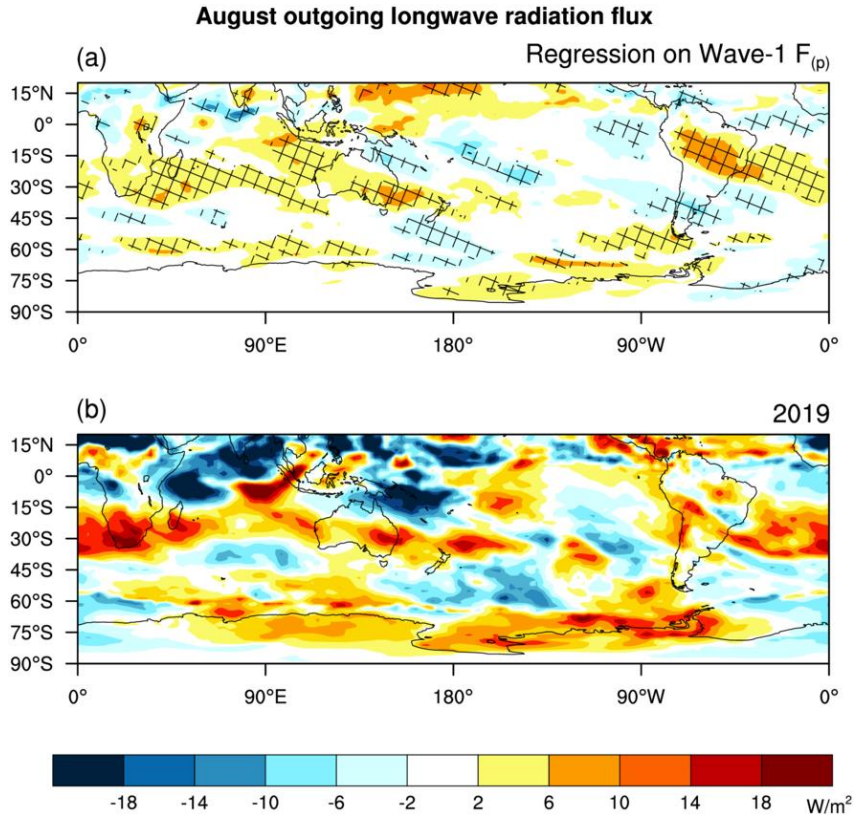

FIG S6. (a) As in Fig. S5b except for the August-mean 2019 outgoing longwave radiation (OLR) anomalies. (b) The observed OLR anomalies of August-mean 2019. The color shading interval is 4 Wm^{-2}. Hatching in (a) indicates statistical significance of the regression coefficients at the 10% level, assessed by a two-tailed Student t-test with 40 samples. 1) A zonal tripole anomaly of convection, consisting of enhanced convection (reduced OLR) in the equatorial western Indian Ocean, reduced convection in the equatorial eastern Indian Ocean and enhanced convection in the far western Pacific to the northeast of Australia; and 2) meridional dipole-like anomalies over the tropical and subtropical south Atlantic Ocean and south Indian Ocean are common features in the OLR pattern in the synthesis of 2019 based on the regression onto the wave-1 northward heat flux at 700 hPa and in August 2019.

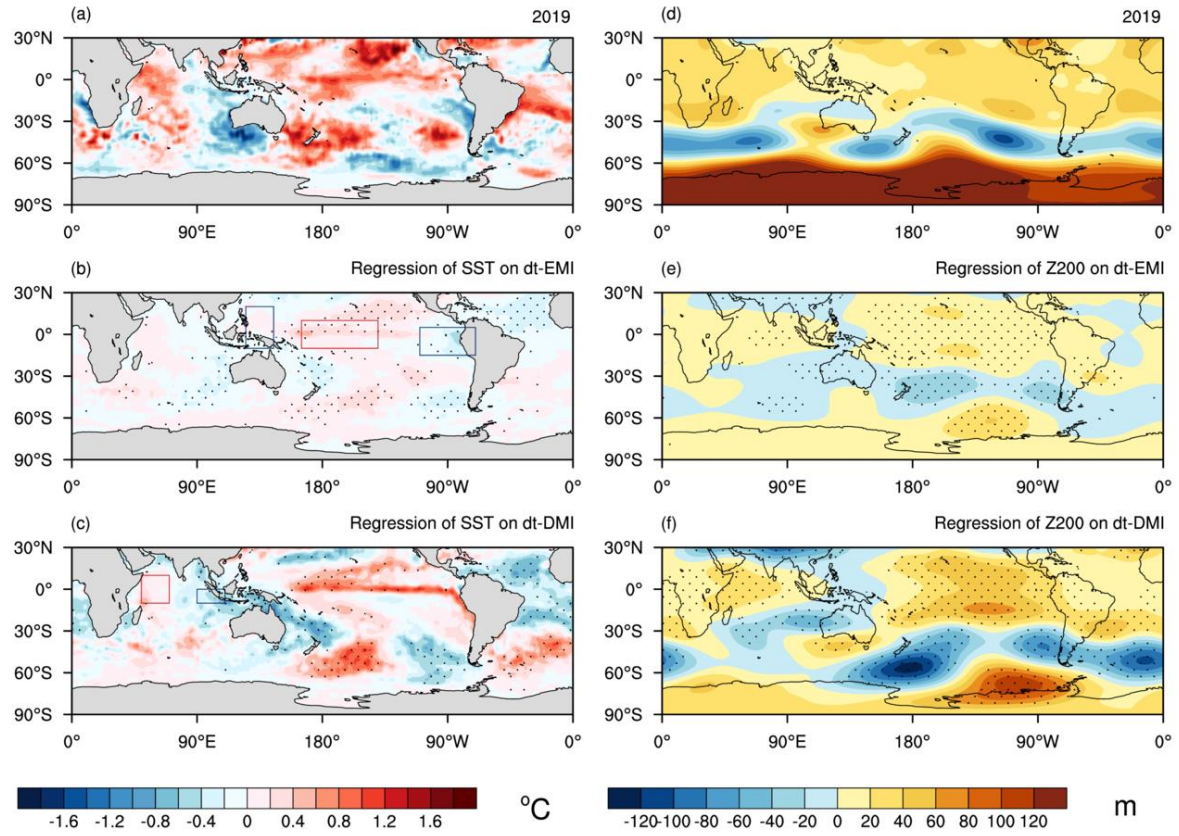

FIG S7. (Left panels) Sea surface temperature (SST) anomalies for October to December (OND) mean (a) observed in 2019; and synthesized by regression onto (b) the de-trended El Nino Modoki Index (EMI; Ashok et al. 2007) and (c) the de-trended Dipole Mode Index (DMI; Saji et al. 1999) as described in the first section of this supplementary document. The EMI monitors the variability of Central Pacific (CP) El Nino whose maximum SST warming is located over the dateline (red box in (b)), being flanked by cooler SSTs in its far west and east (blue boxes in (b)). The DMI monitors the variability of the Indian Ocean Dipole (IOD) mode. The positive IOD is characterized by anomalous cooling in the tropical eastern Indian Ocean (blue box in (c)) and warming in the tropical western Indian Ocean (red box in (c)). (Right panels) (d-f) Same as (a-c) except showing for 200 hPa geopotential height (Z200) anomalies, respectively. The de-trended EMI and DMI were used to highlight the SST and Z200 anomalies explained by the natural modes of tropical SST variability. The color shading interval is 0.2 °C for SST anomalies and 20 m for Z200 anomalies. Stippling in the regression plots indicates statistical significance of the regression coefficients at the 10% level, assessed by a two-tailed Student t-test with 40 samples.

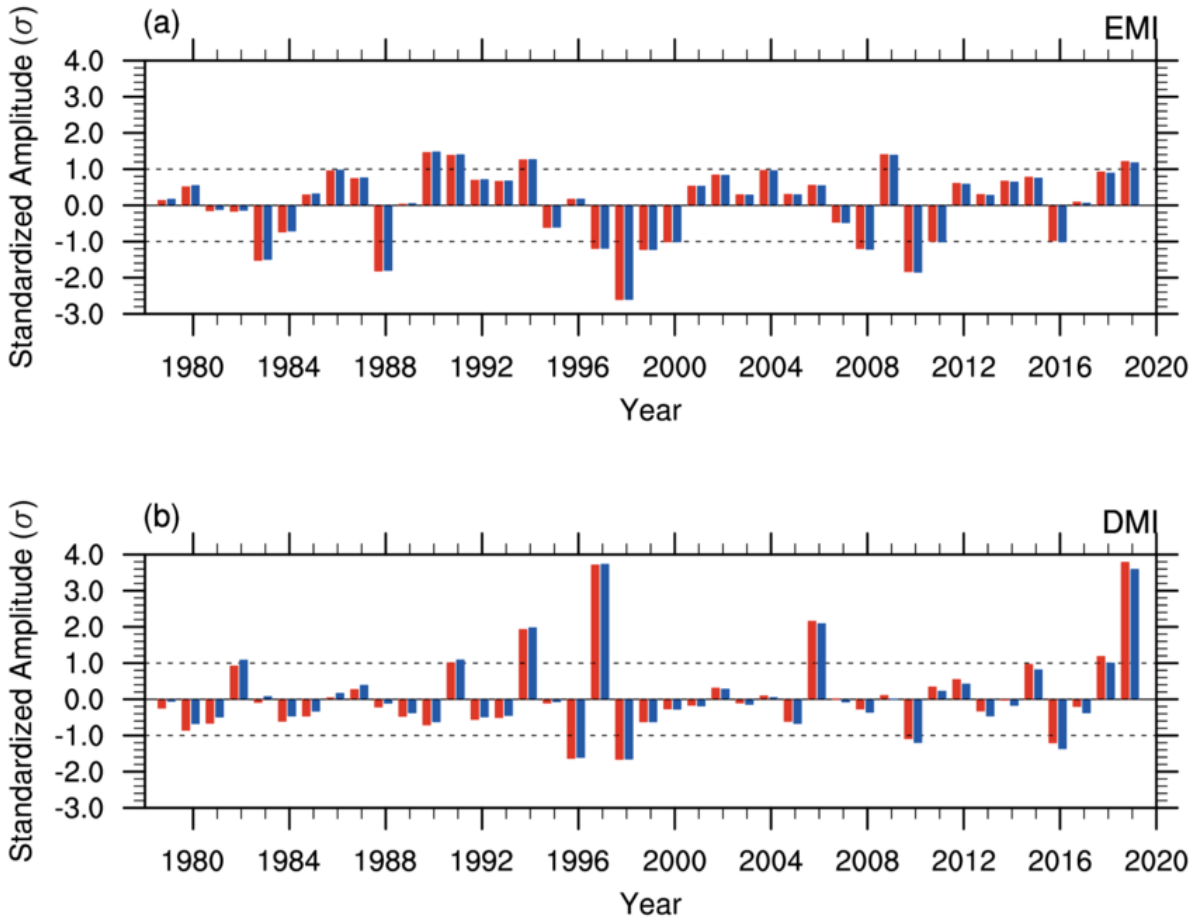

FIG S8. (a) October-December mean (OND) El Nino Modoki Index (EMI; red bars) and de-trended EMI (blue bars). (b) Same as (a) but OND Indian Ocean Dipole Mode Index (DMI). The indices were obtained from SST data from Hurrell et al. (2008) for 1979-1981 and Reynolds et al. (2002) for 1982-2019.

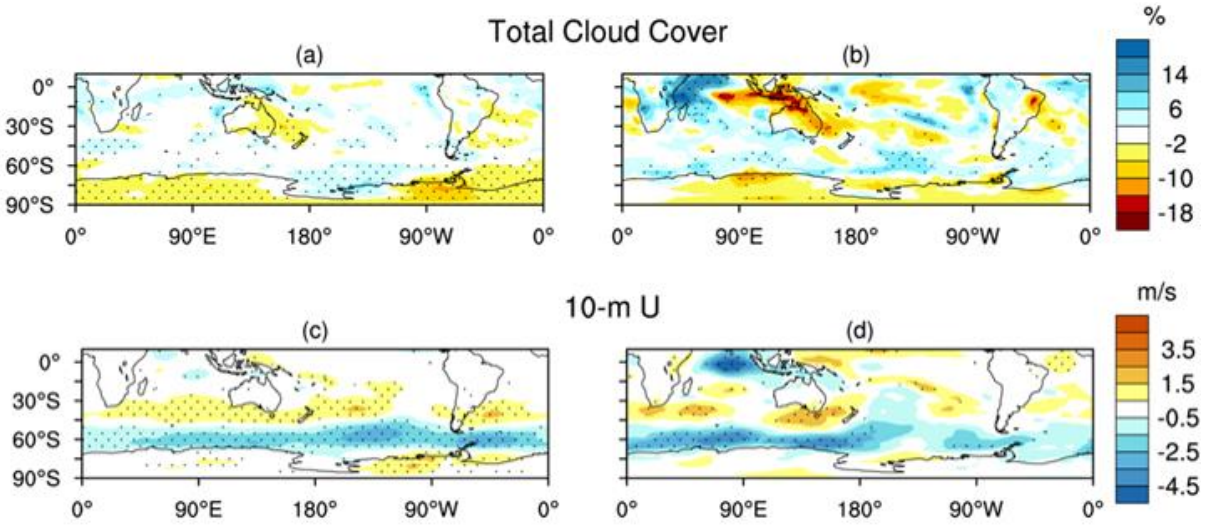

FIG S9. (Left panels) Syntheses of the 2019 OND mean (a) total cloud cover in fraction and (c) 10-m zonal winds derived from the regression onto the SPVI defined in the caption of FIG S2. (Right panels) (b), (d) Respective observed anomalies during OND 2019. The color shading interval in (a) and (b) is 4% and in (c) and (d) is 1 ms^{-1}. Stippling in the left panels indicates statistical significance of the regression coefficients at the 10% level. Stippling in the right panels indicates observed anomalies in the 5% tails of the climatological distribution (1979-2018).

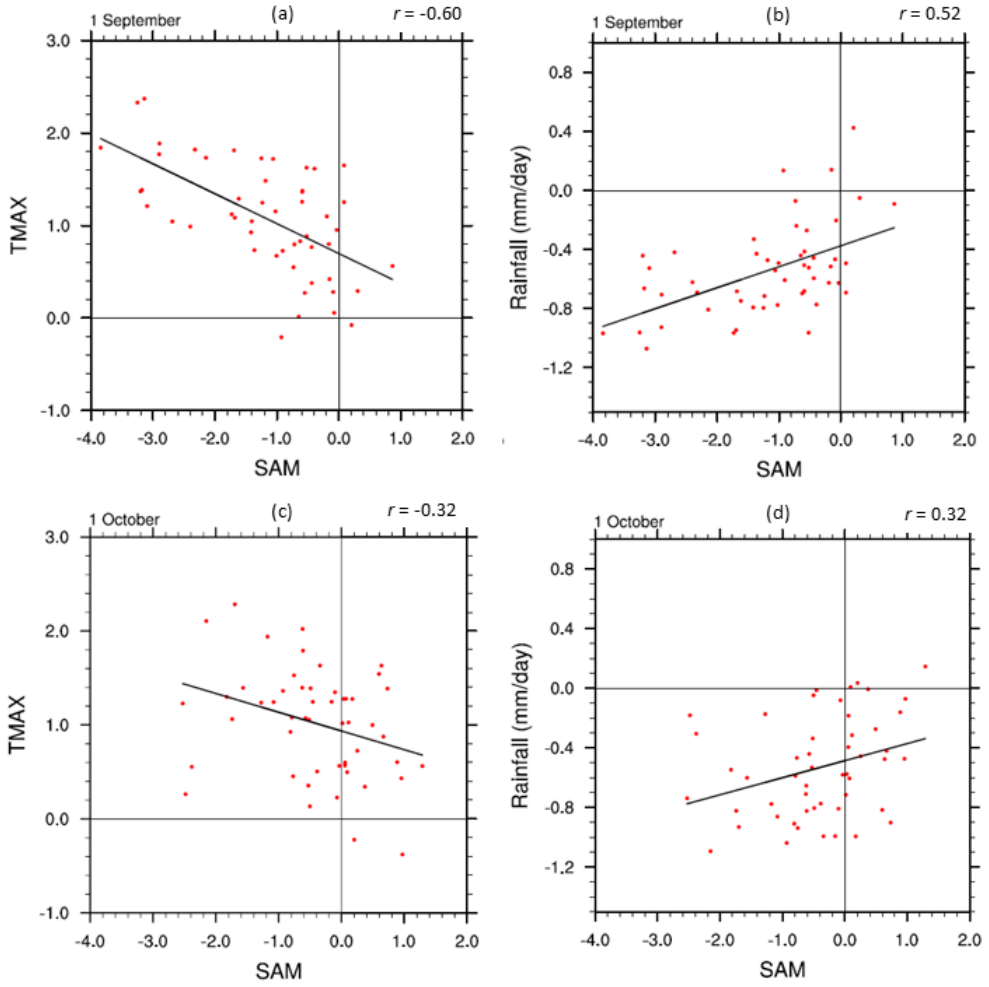

FIG S10. Scatter of the predicted October to December (OND) mean Southern Annular Mode (SAM, standardized units) and eastern Australian (left) maximum temperature (TMAX; °C) and (right) rainfall (mm/day) anomalies. The plots in the top row are for forecasts initialized on 1 September 2019 and in the bottom row are for forecasts initialized on 1 October 2019. The dots are the individual ensemble members (51) from the ECMWF-SEAS5 forecast system. The forecast SAM values were computed by the normalized MSLP difference between 40°S and 65°S following Gong and Wang (1999)'s definition. Eastern Australian TMAX and rainfall were computed as the areal mean land points east of 140°E and over 10°-45°S. The black lines are the linear least square best fit and the associated correlation coefficient is displayed in the upper right of each panel.

References

Ashok, K., S. K. Behera, S. A. Rao, H. Weng, and T. Yamagata, 2007: El Niño Modoki and its possible teleconnection. *J. Geophys. Res. Ocean.*, **112**, doi:10.1029/2006JC003798.

Byrne, N. J., and T. G. Shepherd, 2018: Seasonal persistence of circulation anomalies in the Southern Hemisphere stratosphere and its implications for the troposphere. *J. Clim.*, **31**, 3467–3483, doi:10.1175/JCLI-D-17-0557.1.

Gong, D., and S. Wang, 1999: Definition of Antarctic Oscillation index. *Geophys. Res. Lett.*, **26**, 459–462, doi:10.1029/1999GL900003. http://doi.wiley.com/10.1029/1999GL900003.

Harnik, N., R. K. Scott, and J. Perlwitz, 2005: Wave reflectiom and focusing prior to the major stratospheric warming of September 2002. *J. Atmos. Sci.*, **62**, 640–650, doi:10.1175/JAS-3327.1.

Hurrell, J. W., J. J. Hack, D. Shea, J. M. Caron, and J. Rosinski, 2008: A new sea surface temperature and sea ice boundary dataset for the community atmosphere model. *J. Clim.*, **21**, 5145–5153, doi:10.1175/2008JCLI2292.1.

Lim, E.-P., H. H. Hendon, and D. W. J. Thompson, 2018: Seasonal evolution of stratosphere-troposphere coupling in the Southern Hemisphere and implications for the predictability of surface climate. *J. Geophys. Res. Atmos.*, **123**, 12,002–12,016, doi:10.1029/2018JD029321. http://doi.wiley.com/10.1029/2018JD029321.

Newman, P., and E. Nash, 2005: The unusual Southern Hemisphere stratosphere winter of 2002. *J. Atmos. Sci.*, **62**, 614–628, doi:10.1175/JAS-3323.1. http://journals.ametsoc.org/doi/abs/10.1175/JAS-3323.1.

Peixoto, J. P., and A. H. Oort, 1992: *Physics of Climate*. 1st ed. AIP-Press, XXXIX, 520 pp.

Reynolds, R. W., N. A. Rayner, T. M. Smith, D. C. Stokes, and W. Wang, 2002: An improved in situ and satellite SST analysis for climate. *J. Clim.*, **15**, 1609–1625, doi:10.1175/1520-0442(2002)015<1609:AIISAS>2.0.CO;2.

Saji, N. H., B. N. Goswami, P. N. Vinayachandran, and T. Yamagata, 1999: A dipole mode in the tropical Indian Ocean. *Nature*, **401**, 360–363, doi:10.1038/43854. http://www.nature.com/nature/journal/v401/n6751/full/401360a0.html%5Cnhttp://www.nature.com/nature/journal/v401/n6751/pdf/401360a0.pdf.